Progress In Electromagnetics Research, PIER 15, 141–164, 1997

THREE-DIMENSIONAL SUBTERRANEAN TARGET IDENTIFICATION BY USE OF OPTIMIZATION TECHNIQUES

J. Björkberg and G. Kristensson

1. Introduction

In geophysical prospecting one often ends up trying to solve an inverse problem. In this paper one class of such problems is addressed where a typical prospecting situation is simulated.

When an area with indications of mineable ores is found the prospecting usually enters a phase of extensive subsurface probing by means of long bore holes in order to establish the location, quality and extent of the ores. These bore holes provide the information needed to make the decision of how and if to mine an outcrop. However, it is very expensive and time consuming to drill these holes. It is therefore of vital interest to minimize the number of holes and to optimize their distribution.

Thus the problem that is approached in this paper is; is it possible to determine the size, location and orientation of an ore by making scattering experiments on the surface of the ground or in a nearby bore hole? Furthermore, since real data are always more or less contaminated with noise, it is important to determine how well a recon-

struction can be made in such a case.

Without any a priori information about the size or shape of the ore the problem is not well posed. To stabilize the numerical algorithm some regularization of the problem has to be introduced. This can be made by a restriction of the form of the subterranean inhomogeneity. Since most sulphide ore bodies in Northern Sweden are very thin compared to their lateral extensions an appropriate model for these is to approximate them with a thin, perfectly conducting, elliptic disk.

The scattering domain under consideration consists of a halfspace with an overburden. Submerged in the halfspace is a perfectly conducting elliptic disk which models the target ore. The scattering domain is excited by a time-harmonic field emitted by a loop antenna on the ground and the total field or the scattered field is calculated along a bore hole or in a mesh on the surface of the ground. In total, there are eleven free parameters in the model. The scatterer is described by the size, aspect ratio, location of the center, and the three Euler angles. The halfspace is described by its resistivity, and the overburden by its thickness and resistivity. The span of these free parameters constitute the parameter space of the problem.

In this model the forward problem can be stated. Given a point x in the parameter space, find the field values d at the prescribed field points, i.e.,

$$m(x) = d$$

where the function m is non-linear. This forward problem is solved with the null-field approach which is further described in the appendix.

The corresponding inverse problem is now stated. Given a set d of data, find the corresponding point x in the parameter space for which $m(x)$ gives an optimal fit to the data in some suitable norm. This inverse problem is solved with a data fitting procedure of Newton type.

2. Optimization Techniques

In this section the optimization techniques used are presented. Optimization techniques have been used extensively to solve inverse problems. An overview of the use of optimization techniques to solve electromagnetic inverse problems can be found in [6]. For an extensive

presentation of optimization based on the Newton method the reader is referred to [3].

The optimization problem is to fit a set of data $(y_i, d_i), i = 1, \ldots, m$, with a model $M(x, y)$. Here $x \in \mathbf{R}^n$ is a point in the parameter space, y_i are the space coordinates of the $i : th$ "measurement" and d_i is the data of the same. It is convenient to introduce a residual function

$$R : \mathbf{R}^n \to \mathbf{R}^m \quad , \quad m > n$$

whose components are defined as

$$r_i(x) = M(x, y_i) - d_i \quad , \quad i = 1, \ldots, m$$

Given this residual function, the problem at hand can be written as a minimization problem

$$\min_{x \in \mathbf{R}^n} f(x) = \min_{x \in \mathbf{R}^n} \frac{1}{2} R^T(x) R(x) = \min_{x \in \mathbf{R}^n} \frac{1}{2} \sum_{i=1}^{m} r_i(x)^2$$

This problem is normally referred to as the nonlinear least-squares problem.

One possible approach to solve the nonlinear least-squares problem is to make an affine model $M_c(x)$ of $R(x)$ around the current point x_c, i.e.,

$$M_c(x) = R(x_c) + J(x_c)(x - x_c) \tag{2.1}$$

where $J(x)_{ij} = \partial r_i(x)/\partial x_j$ is the Jacobian. Normally, one can not expect to find an x_+ such that $M_c(x_+) = 0$ since it is an overdetermined system. ($M_c : \mathbf{R}^n \to \mathbf{R}^m, \quad m > n$). One classic approach to this problem is to choose x_+ as the minimizer of the linear least-squares problem

$$\min_{x \in \mathbf{R}^n} \frac{1}{2} ||M_c(x)||_2^2$$

If $J(x_c)$ has full rank the solution can be written as

$$x_+ = x_c - \left[J^T(x_c) J(x_c) \right]^{-1} J^T(x_c) R(x_c) \tag{2.2}$$

Methods based on this iterate are referred to as Gauss-Newton type methods.

One complication with the Gauss-Newton method is that the Jacobian might be very ill-conditioned, reflecting the fact that the model is insensitive to variations in certain directions in the parameter space.

In order to overcome this we will make a different use of the affine model (2.1). This approach is based on the singular value decomposition (SVD) of the Jacobian matrix ($J \in \mathbf{R}^{m\times n}$)

$$J = UDV^T$$

Here $U \in \mathbf{R}^{m\times m}$ and $V \in \mathbf{R}^{n\times n}$ are orthogonal matrices. The matrix $D \in \mathbf{R}^{m\times n}$ is diagonal with its entries defined by $d_{ii} = \mu_i \geq 0$, $i = 1, \ldots, \min(m, n)$, $d_{ij} = 0, i \neq j$. The μ_i 's are called the *singular values* of J . Given the SVD of J , it is possible to define a generalized inverse, the Moore-Penrose inverse, as

$$J^\dagger = VD^\dagger U^T \quad , \quad D^\dagger = \begin{cases} d_{ii}^\dagger = \begin{cases} 1/\mu_i, & \mu_i > 0 \\ 0, & \mu_i = 0 \end{cases} \\ d_{ij}^\dagger = 0, & i \neq j \end{cases}$$

Through this generalized inverse $M_c(x) = 0$ has a *unique* solution

$$x_+ = x_c - J^\dagger(x_c)R(x_c)$$

This iterate is called the SVD-Newton iterate.

The Moore-Penrose inverse also provides a natural way to regularize the problem. This is due to the following; if the problem is insensitive to variations in one of the parameters, or a linear combination of parameters, this means that the column vectors of the Jacobian has a high degree of linear dependence and the condition number of the matrix is very high. In terms of the SVD, this implies that the matrix has one or more very small singular values. The condition number κ is in fact defined as $\kappa = \mu_{max}/\mu_{min}$. The idea is to suppress this linear dependence of the column vectors, thus making the matrix better conditioned. This is done by introducing a regularizing parameter λ and to define a regularized Moore-Penrose inverse through

$$J_\lambda^\dagger = VD_\lambda^\dagger U^T \quad , \quad D_\lambda^\dagger = \begin{cases} d_{ii}^\dagger = \begin{cases} 1/\mu_i, & \mu_i \geq \lambda^2 \\ 0, & \mu_i < \lambda^2 \end{cases} \\ d_{ij}^\dagger = 0, & i \neq j \end{cases}$$

The regularizing parameter has the effect of masking off directions in the parameter space in which the problem is ill-conditioned.

The strategy is to start the optimization with some $\lambda > 0$, large enough to make the Jacobian $J_\lambda^\dagger$ well behaved. In this way a point x_λ is found which minimizes the rms-error of the residuals for the affine model and which is hopefully near the true minimizer x_* of the problem. Then the parameter λ is decreased, making the Jacobian more ill-conditioned. But since x_λ is close to x_*, the algorithm is in a better position to handle this. This procedure is repeated until the minimizer x_* is found. In this way the search is guided down to the minimizer. Keeping the Jacobian well behaved while x_c is far away from the minimizer x_*, saving the difficult parts until x_c is close to x_*.

If the data are clean, then reducing λ will decrease the rms-error of the datafit, monotonically, eventually making $x_\lambda \to x_*$ as $\lambda \to 0$. If, however, the data are contaminated with noise, then the rms-error might actually increase as λ gets very small. In such a case, the procedure is stopped at the optimal λ which gives the best fit. The problem of choosing the optimal λ is in general tractable.

All variations of the Newton iteration are based on making a local model around the current point. Hence, these methods are at best locally convergent and have to be augmented with a global strategy in order to achieve global convergence. The SVD-Newton step (2) might actually fail to be a descent step in certain situations, e.g. if the problem at hand is not a small residual problem or the problem is very nonlinear. In such situations the step might be too long and that the optimal minimizer within the range of the Newton step might be located in a slightly different direction.

In this paper, a backward line tracing strategy is chosen. This is done as follows: First the Newton step is tried. If this step gives an acceptable decrease in residual, it is accepted. If not, a backtracing along the Newton direction is employed. Other strategies, i.e., trust region approaches, are possible [3].

3. Results

In this section the performance of the algorithm is presented by a number of numerical calculations. The performance is compared for different types of data, i.e., bore hole measurements or surface grid measurements, and the sensitivity of the reconstruction to error in the data is investigated.

It is natural to separate the total field into a regional field and an anomalous field. The term regional field refers to the field scattered from large-scale structures, such as layering, with no target ore present. By anomalous field is understood the scattered field due to the presence of the target ore. This break up of the field enters in a natural way in the forward solver (A.16–A.18). In prospecting situations there are often a priori information about the regional structures and their physical properties, which can be utilized to separate the total field. In general though it is a nontrivial problem to extract the anomalous field. The first reconstructions are made with anomalous field data, i.e., it is assumed that the total field is properly separated into a regional and an anomalous field. The more general problem of both separating the field and reconstructing the target as well as the regional parameters is addressed at the end of this section.

The first class of reconstructions to be presented uses data along a bore hole. At each field point the data consist of all three components of the anomalous field, both magnitude and phase information.

The coordinate system used to describe the geometry has its origin at the point where the bore hole penetrates the surface. The x-axis is directed towards the center of the loop antenna and the z-axis is directed upward. The bore hole is parametrized by the spherical angles η and ψ, and the length l along the hole. The antenna is characterized by the coordinates of the center $(x_t, 0, 0)$, and the radius r_t. The scattering geometry is shown in Figure 1. The target scatterer, the elliptic disk, is characterized by the length of the half axes a and b. The center of the scatterer is given by (x_s, y_s, z_s) and the orientation of the scatterer is given by the Euler angles α, β and γ. Here α is a rotation around the z-axis, β a rotation around the y'-axis, and γ a rotation around the z''-axis [1]. The disk-related parameters are shown in Figure 2.

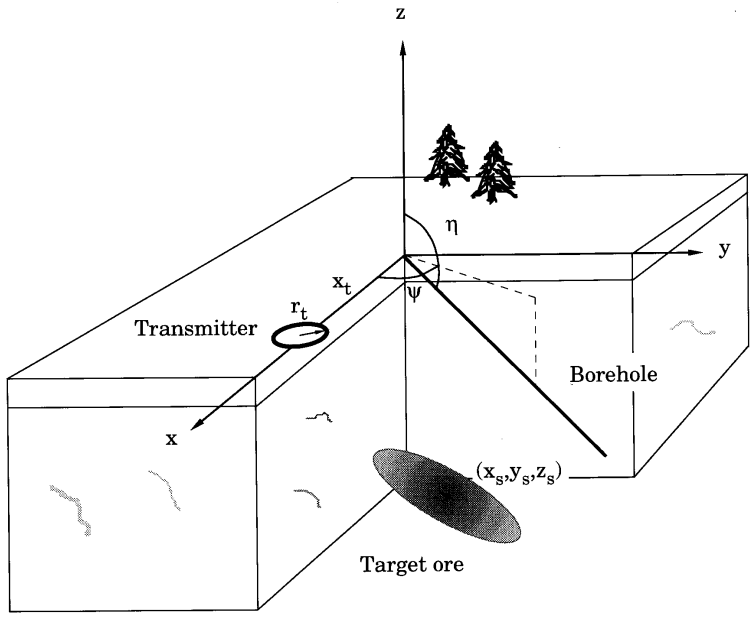

Figure 1. The scattering geometry.

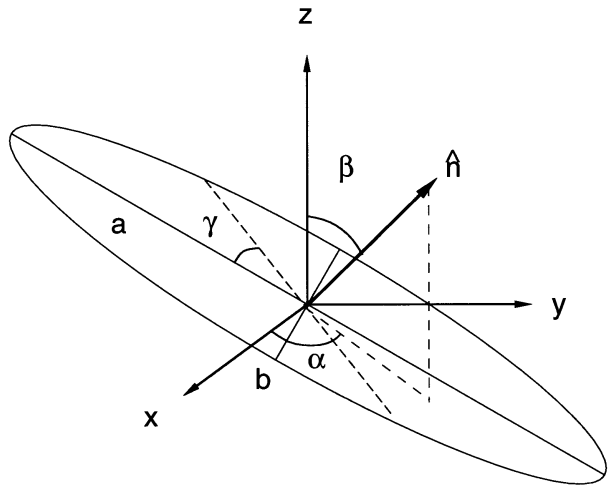

Figure 2. The size of the elliptic disk is given by the half axes a and b, and the orientation of the disk given by the Euler angles α, β and γ.

In the computations to follow, the free parameters of the second column of Table 1 are used to calculate the synthetic data. The source is located at $x_t = 800\,m$, its working frequency $20\,kHz$ and the radius $r_t = 100\,m$. The field points are situated along a bore hole, in the direction $\eta = 150°$ and $\psi = -45°$. In total 25 field points, every 15th meter starting at $l = 100\,m$, are used.

Parameter	*Correct value*	*Initial guess*
x_s	400 m	360 m
y_s	-100 m	-130 m
z_s	-250 m	-280 m
a	100 m	130 m
b	25 m	50 m
α	45 *deg*	35 *deg*
β	30 *deg*	10 *deg*
γ	60 *deg*	50 *deg*

Table 1. Free parameters

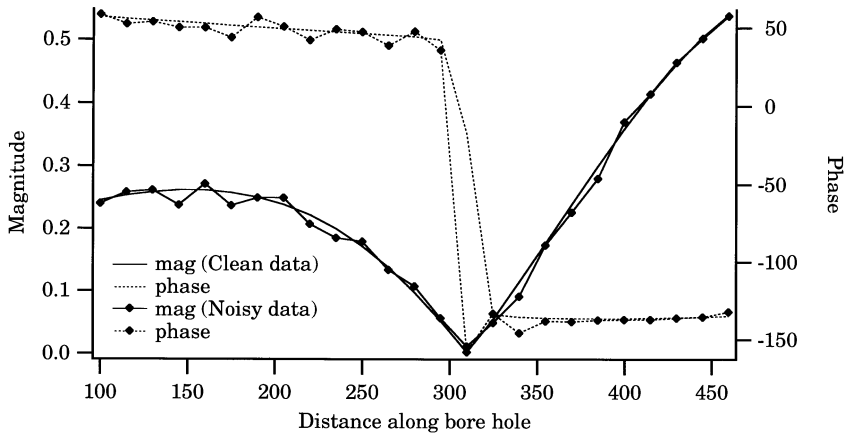

Figure 3. X **component of synthetic data (H-field) along the bore hole. The field is normalized by a factor** $Mk_o^3/4\pi$**. The lines without markers show the magnitude (solid line) and phase (broken line) of the clean data. The lines with markers show the corresponding noise contaminated data. These data are contaminated with Gaussian noise with zero mean and standard deviation** $\sigma = 0.015$**.**

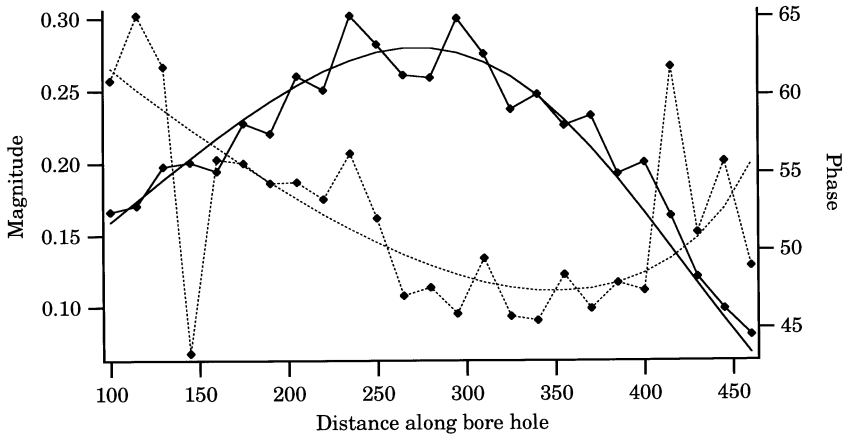

Figure 4. Y **component of synthetic data along the bore hole. All other parameters are the same as in Figure 3.**

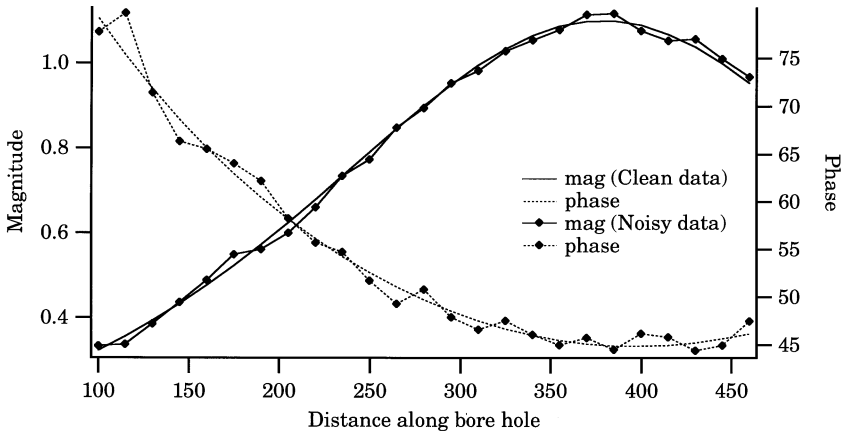

Figure 5. Z **component of synthetic data along the bore hole. All other parameters are the same as in Figure 3.**

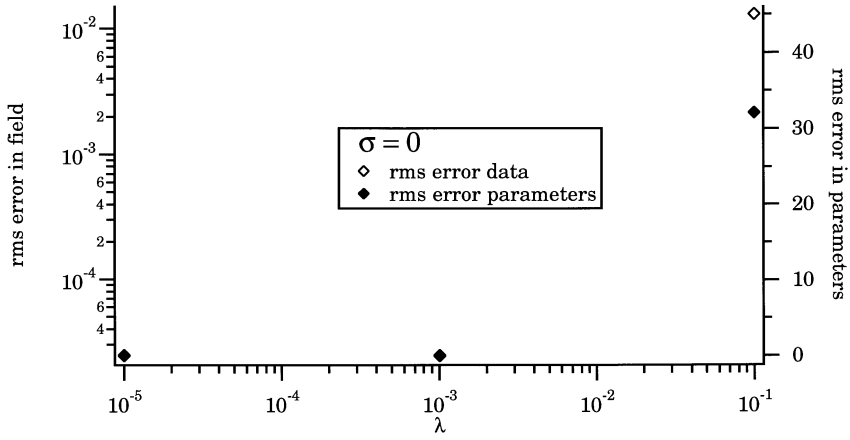

Figure 6. The left axis shows the rms error of the field values for three different values of the regularization parameter λ in a logarithmic scale. The right axis shows the corresponding rms error of the parameters in a linear scale. The data are clean.

All the reconstructions start from the initial guess listed in the third column of Table 1. The first reconstruction, in the following called experiment 1, is done using clean data. The magnetic field is normalized by a factor $Mk_o^3/4\pi$, where M is the magnetic moment of the source and k_o is the wavenumber of free space. The initial data is shown in Figures 3–5. In these figures the magnitude of the clean data is shown as the solid line without markers and the phase as the broken line without markers, respectively. As is seen in Figure 6 the rms error decreases monotonically as the regularizing parameter λ decreases. This is an indication that the problem is fairly well-posed. In Table 2 the very fast local convergence is manifested. After just a few iterations the algorithm converges to the minimizer.

Exp 1		
λ	*# iterations*	*rms error*
0.1	5	$1.29\,10^{-2}$
0.01	5	$2.43\,10^{-5}$
0.001	1	$2.42\,10^{-5}$

Table 2. Iterations of experiment 1.

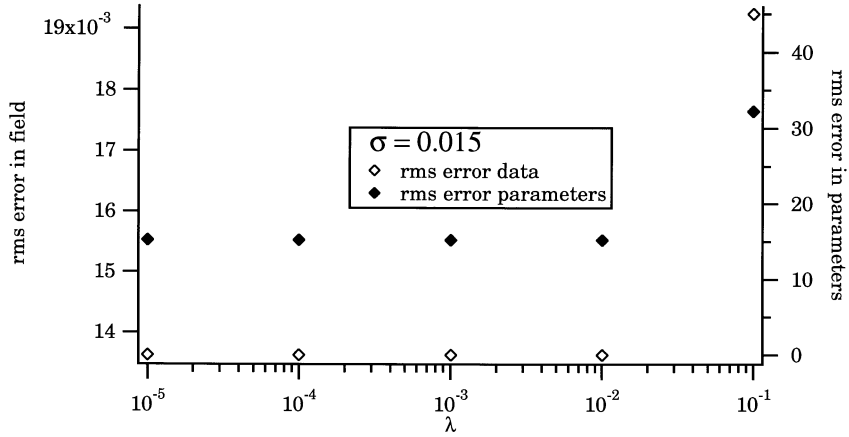

Figure 7. Same as Figure 6 but the data are contaminated with Gaussian noise with zero mean and standard deviation $\sigma = 0.015$. Both left and right axes show the rms errors in linear scales.

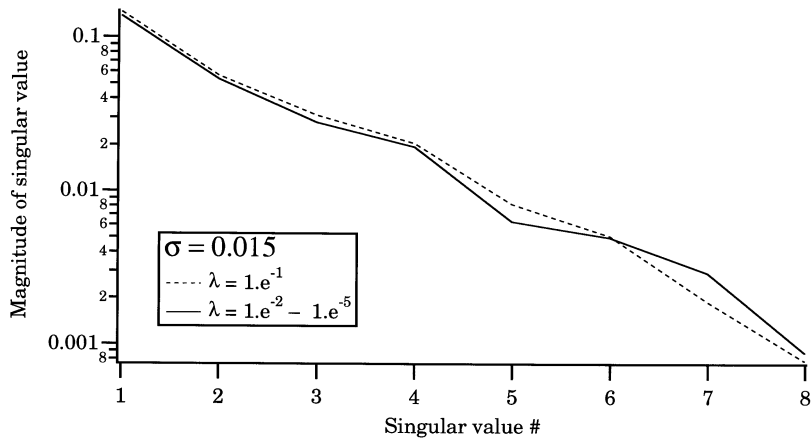

Figure 8. The magnitude of the singular values for five different values of the regularizing parameter λ. Note the slow and even decrease of the singular values.

In the following experiments the data are contaminated with noise. The noise is assumed to be generated by an independent noise source which is modelled by Gaussian noise with zero mean and standard deviation σ, where σ is independent of the original data. In

experiment 2 σ is equal to 0.015. The magnitude and the phase of the contaminated data are shown in Figures 3–5, as marked solid lines and marked broken lines, respectively. The convergence of the algorithm with these data is shown in Figure 7, where the rms error of the datafit, left axis, and the rms error of the parameterfit, right axis, are plotted versus the regularizing parameter λ. As demonstrated in the figure, the algorithm quickly converges to the true minimizer even in this case. The well-behavedness of the algorithm for bore hole data is further manifested by the slow decrease in magnitude of the singular values, as shown in Figure 8.

As a final worst case the bore hole data is contaminated with Gaussian noise with a standard deviation σ equal to 0.05. The input data of this experiment, No. 3, is shown in Figures 9–11. As in Figures 3–5, the marked solid lines and the marked broken lines show the magnitude and phase of the error contaminated data, respectively. As seen in the figure the quality of the input data is quite bad in this case. Still the algorithm gives an acceptable reconstruction. In Figure 12 the convergence for this noise level is demonstrated, and in Figure 13 the decrease of the singular values.

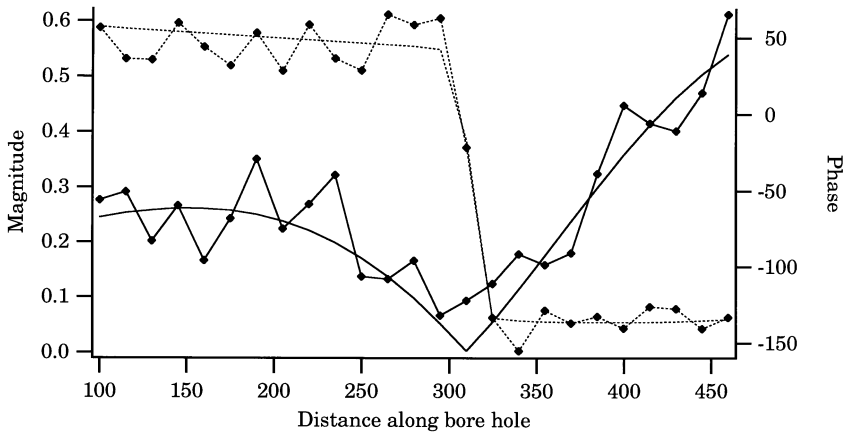

Figure 9. X **component of synthetic data along the bore hole. The lines without markers show the magnitude (solid line) and phase (broken line) of the clean data. The lines with markers show the corresponding noise contaminated data. These data are contaminated with Gaussian noise with zero mean and standard deviation** $\sigma = 0.05$**.**

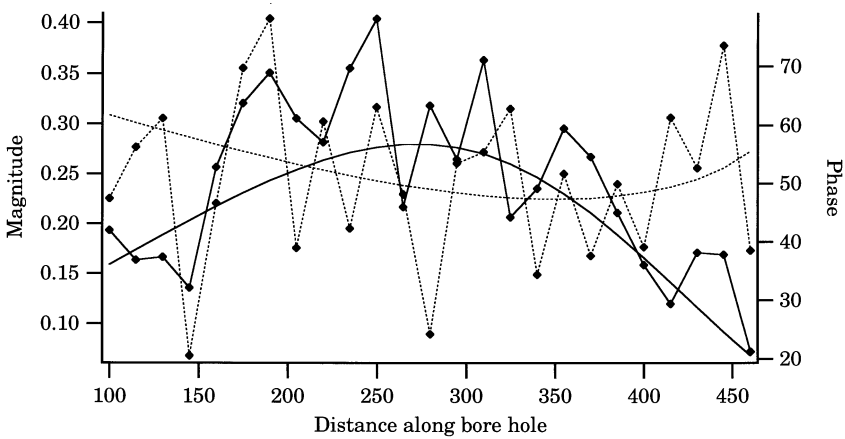

Figure 10. Y **component of synthetic data along the bore hole. All other parameters are the same as in Figure 9.**

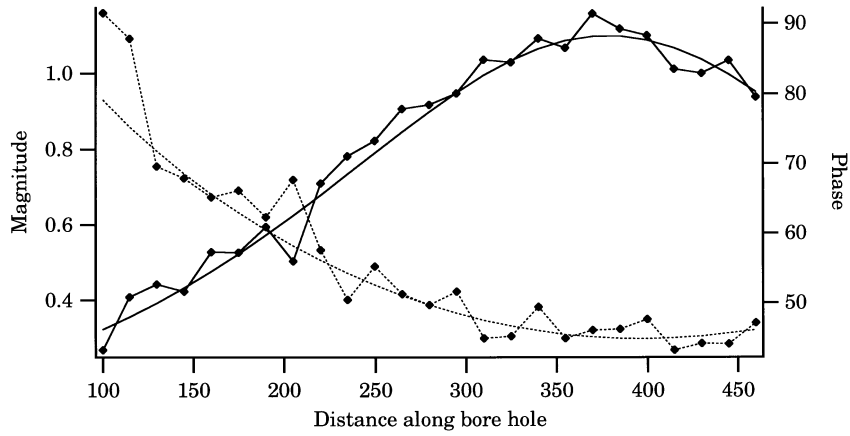

Figure 11. Z **component of synthetic data along the bore hole. All other parameters are the same as in Figure 9.**

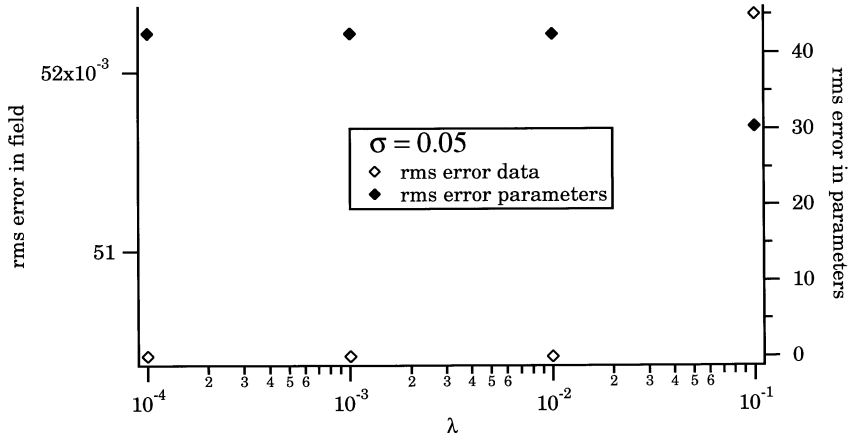

Figure 12. Same as Figure 7 but the data are contaminated with Gaussian noise with zero mean and standard deviation $\sigma = 0.05$.

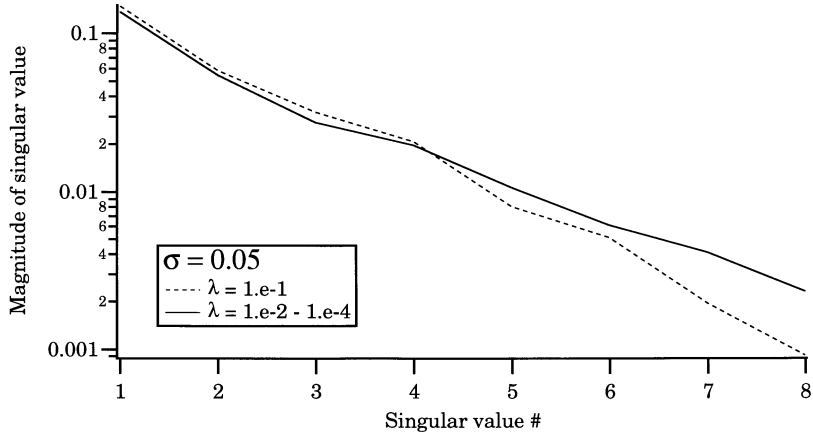

Figure 13. Same as Figure 8 but the standard deviation of the Gaussian noise is $\sigma = 0.05$.

Next set of experiments presented uses data collected on the ground surface. Two different meshes are used. The first consists of three parallel lines running $40m$ apart from each other. Along each line seven measurements are made each 20th meter. The second layout has two more lines placed between the three original lines. Thus, in this

layout the inter line distance is $20m$. In both layouts the scatterer is placed $60m$ out along the center line and straight below the same. All other parameters of the scatterer and the ground are the same as in the bore hole case.

With clean data the algorithm makes good reconstructions with both layouts. The convergence of the algorithm in the case of clean data is shown in Figure 14, where the rms error of the datafit and the parameter fit are shown for different λ. In this figure the five line layout is used. The three line layout gives the same output.

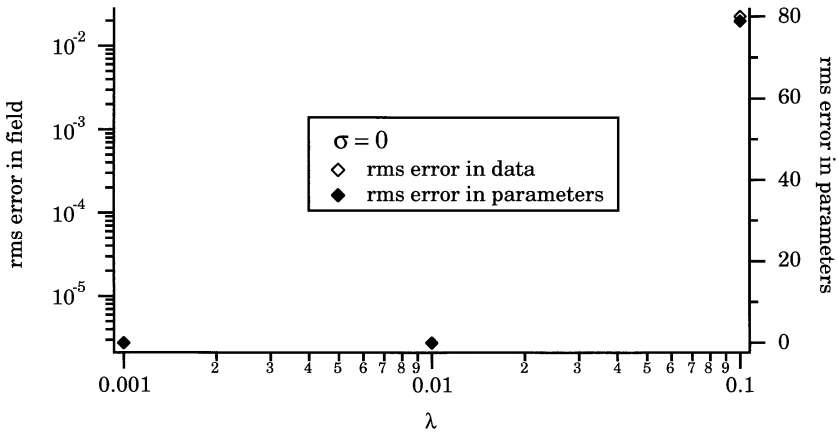

Figure 14. Same as Figure 6 with clean data for a surface layout. The layout consists of 5 parallel lines 20m apart and with 7 measurements each 20th m along each line.

In the case of noise contaminated data the surface layouts do not behave as well as in the bore hole case. In Figure 15 the singular values are shown for noise contaminated data with $\sigma = 0.0015$. Note that the standard deviation of the noise in this case is one order of magnitude smaller compared to experiment 2. The quality of the reconstruction with noise contaminated data with standard deviation $\sigma = 0.0015$ and a surface layout with five lines, experiment 4, is shown in Figure 16.

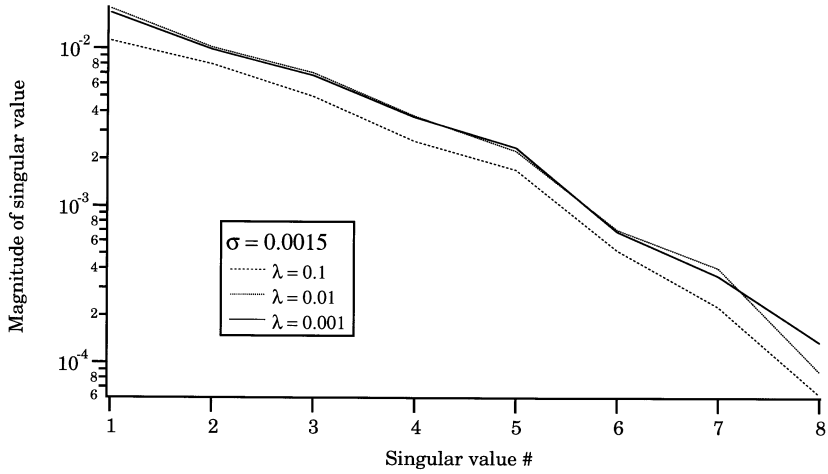

Figure 15. The figure shows the magnitude of the singular values for different λ. The data are collected in the same surface layout as in Figure 14.

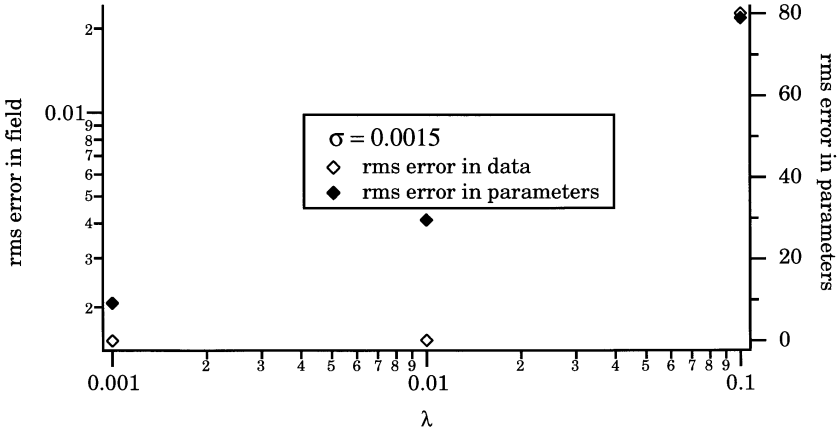

Figure 16. Same as Figure 6 but the standard deviation of the Gaussian noise is $\sigma = 0.0015$.

So far all reconstructions are made using anomalous field data. Thus it is assumed that the total field can be separated into a regional field and an anomalous field by some means. In general this is a non-trivial problem which has to be addressed. One of the main difficulties

is that the magnitude of the anomalous field is typically only a small fraction of the total field. This characteristic tends to make the extraction of the anomalous field sensitive to noise. The reconstruction of the target parameters is very sensitive to a bias (i.e., a systematic error) in the anomalous field, due to incorrect separation of the total field into regional and anomalous fields, respectively. It is therefore of vital importance that the reconstruction of the regional parameters be accurate. In the previous reconstructions no bias occurs since Gaussian noise with zero mean is used. Thus this type of noise is much more well-behaved.

One approach to separate the fields is to use an iterative scheme. At each step the regional field is approximated by the difference between the total field and the optimized anomalous field from the previous iteration. The regional parameters are then determined by an optimization to this field. In the same way the anomalous field is approximated as the difference between the total field and the optimized regional field found above, and the new set of target parameters are determined by an optimization to this field.

This process is repeated until convergence is reached. Noting that the regional field constitutes the major part of the total field; the total field itself is used as a first approximation to the regional field. Symbolically the iteration process can be written as

$$
\begin{aligned}
&\begin{cases} \boldsymbol{H}^0_{\text{reg}} &= \boldsymbol{H}_{\text{tot}} &\rightarrow \boldsymbol{H}^0_{\text{reg,opt}} \\ \boldsymbol{H}^0_{\text{anom}} &= \boldsymbol{H}_{\text{tot}} - \boldsymbol{H}^0_{\text{reg,opt}} &\rightarrow \boldsymbol{H}^0_{\text{anom,opt}} \end{cases} \\
&\begin{cases} \boldsymbol{H}^1_{\text{reg}} &= \boldsymbol{H}_{\text{tot}} - \boldsymbol{H}^0_{\text{anom,opt}} &\rightarrow \boldsymbol{H}^1_{\text{reg,opt}} \\ \boldsymbol{H}^1_{\text{anom}} &= \boldsymbol{H}_{\text{tot}} - \boldsymbol{H}^1_{\text{reg,opt}} &\rightarrow \boldsymbol{H}^1_{\text{anom,opt}} \end{cases} \\
&\quad\vdots \\
&\begin{cases} \boldsymbol{H}^n_{\text{reg}} &= \boldsymbol{H}_{\text{tot}} - \boldsymbol{H}^{n-1}_{\text{anom,opt}} &\rightarrow \boldsymbol{H}^n_{\text{reg,opt}} \\ \boldsymbol{H}^n_{\text{anom}} &= \boldsymbol{H}_{\text{tot}} - \boldsymbol{H}^n_{\text{reg,opt}} &\rightarrow \boldsymbol{H}^n_{\text{anom,opt}} \end{cases}
\end{aligned}
$$

Figure 17 shows the result of the iterative procedure. The geometry is the same as in experiment 1. The data are contaminated with Gaussian noise with $\sigma = 0.01$ but this time the total field is used. As can be seen in the figure the scheme converges to a fix point in the parameter space giving an acceptable reconstruction of both the regional parameters as well as the target parameters.

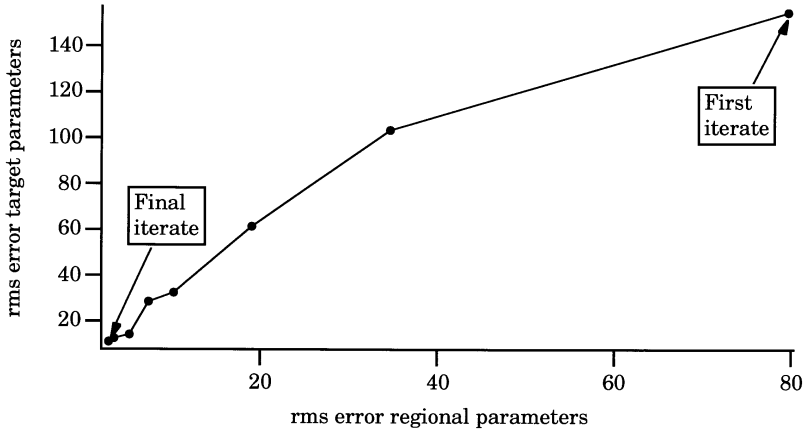

Figure 17. Separation of the total field into a regional field and an anomalous field. The vertical axis show the rms error in the target parameters and the horizontal axis the rms error in the regional parameters.

4. Conclusions

The identification of subterranean metallic ores from scattering experiments is in general not a well-posed problem. However, by restricting the shape of the target the problem is regularized enough to make it numerically stable. In this paper we have modeled the ore by a perfectly conducting elliptic disk, which is a reasonable model for the type of sulphide ores found in Northern Sweden.

Given the assumption that the scattering data can be properly separated into a regional and an anomalous field it is shown that the target can be identified from a feasible starting guess. The algorithm is also shown to be stable to noise for realistically noise contaminated data.

The separation of the scattering data into a regional and an anomalous part is a nontrivial problem. The last part of the article presents a possible way of separating the field and determine the basement parameters as well as the target parameters through an iterative process. The convergence of this process can be improved by providing a priori information about the regional large-scale structures and their physical properties.

Appendix

A. T-matrix formulation and computation of the forward problem

In this appendix a brief description of the method used to solve the forward problem, the null-field method, is given. Since the intention of this appendix is to give the reader an overview rather than a detailed description references to appropriate sources are given where needed. This overview is given in three steps. First the null-field approach is applied to a perfectly conducting three dimensional scatterer. As a second step the regional model, consisting of a half-space covered by an overburden excited by a loop antenna, is considered. Finally these two models are combined into a complete model which takes into account the interactions between the various scattering surfaces [4] (cf. also [5]).

A.1 Null-field approach to 3-d scatterer

The problem is to compute the scattered field, assuming that the geometry of the scatterer and the incident field is known. The initial step in the null-field approach is to expand the fields in suitable sets of global expansion functions. Thus the incident and the scattered fields are expanded in spherical vector waves around an origin inside the scatterer

$$\boldsymbol{E}^{inc}(\boldsymbol{r}) = \sum_n a_n \boldsymbol{v}_n^i(k\boldsymbol{r})$$
$$\boldsymbol{E}^{sc}(\boldsymbol{r}) = \sum_n f_n \boldsymbol{v}_n^e(k\boldsymbol{r})$$

where $\boldsymbol{v}_n^i(k\,\boldsymbol{r})$ and $\boldsymbol{v}_n^e(k\,\boldsymbol{r})$ are the regular and outgoing spherical vector waves, respectively. These waves are defined as

$$\begin{aligned} \boldsymbol{v}_{1\sigma ml}^i &= j_l(kr)\boldsymbol{A}_{1\sigma ml}(\hat{r}) \\ \boldsymbol{v}_{2\sigma ml}^i &= \frac{[kr\, j_l(kr)]'}{kr}\boldsymbol{A}_{2\sigma ml}(\hat{r}) + \sqrt{l(l+1)}\frac{j_l(kr)}{kr}\boldsymbol{A}_{3\sigma ml}(\hat{r}) \end{aligned} \tag{A.1}$$

The outgoing vector waves are defined in a similar way by exchanging

the spherical bessel function j_l with spherical hankel functions of the first kind $h_l^{(1)}$ in (A.1).

Furthermore, the unknown surface field on the scatterer is expanded in tangential vector waves as

$$\boldsymbol{J}(\boldsymbol{r}) = \hat{\nu} \times \boldsymbol{H}(\boldsymbol{r}) = \frac{Y}{k} \sum_{n'} \alpha_{n'} \hat{\nu} \times \left(\nabla \times \boldsymbol{v}^i_{n'}(k\boldsymbol{r}) \right)$$

Here Y is the inverse of the wave impedance, i.e., $Y = k/\omega\mu$.

Between the expansion coefficients a_n and f_n there is a linear relation.

$$f_n = \sum_{n'} T_{nn'} a_{n'}$$

Once the T-matrix is found the scattering problem is solved. The null-field approach provides an algorithm to find a truncated approximation to $T_{nn'}$. This is done by deriving the relations between the incident field and the surface field, and the scattered field and the surface field, i.e.,

$$a_n = -\sum_{n'} Q^e_{nn'} \alpha_{n'} \tag{A.2}$$

$$f_n = \sum_{n'} Q^i_{nn'} \alpha_{n'} \tag{A.3}$$

The entries of the Q^e-matrix are explicitly given by [7], [8]

$$Q^e_{nn'} = k \int_S \left\{ \boldsymbol{v}^e_n(\boldsymbol{r}) \times [\nabla \times \boldsymbol{v}^i_{n'}(\boldsymbol{r})] \right\} \cdot \hat{\nu}\, dS \tag{A.4}$$

The expressions for the Q-matrices of a perfectly conducting ellipsoid, which is the scatterer considered in this paper, are given in [2]. Here it suffices to note that the entries in the matrices are integrations over the surface of the scatterer where the integrands are combinations of the expansion functions. Hence the Q-matrices can be computed explicitly. Once the Q-matrices are computed to a given truncation, the T-matrix is the solution of the matrix equation.

$$TQ^e = -Q^i \tag{A.5}$$

A.2 Stratified ground excited by loop antenna

In the previous section it was natural to use spherical wave functions since the scatterer was a three dimensional object. In the current setting with a stratified ground it is more natural to work with plane vector waves. The reason for this is that the boundary conditions are easy to fulfil with plane waves. A plane wave that impinges on a plane interface gives rise to a reflected plane wave and a transmitted plane wave. The amplitudes are given by the reflection and transmission coefficients, respectively, and the directions of propagation are given by Snell's law. The natural starting point is thus to expand the known incident field and the scattered field in plane waves, i.e.,(cf., e.g., [5])

$$\boldsymbol{E}^{inc}(\boldsymbol{r}) = \sum_{j=1}^{2} \int_{0}^{2\pi} d\beta \int_{C_-} \sin\alpha \, d\alpha a_0(\boldsymbol{k_0}) \boldsymbol{\Phi}_j(\boldsymbol{k_0}; \boldsymbol{r}) \tag{A.6}$$

$$\boldsymbol{E}^{sc}(\boldsymbol{r}) = \sum_{j=1}^{2} \int_{0}^{2\pi} d\beta \int_{C_+} \sin\alpha \, d\alpha b_0(\boldsymbol{k_0}) \boldsymbol{\Phi}_j(\boldsymbol{k_0}; \boldsymbol{r}) \tag{A.7}$$

where $C_\pm$ are integration contours in the complex α-plane chosen in such a way that $k \sin\alpha \in [0, \infty)$. Integration over C_+ refers to up going waves, and C_- to down going waves.

In order to simplify the notation the following convention, introduced in [4], is adopted. Integration and summation over j are suppressed and we write

$$\sum_{j=1}^{2} \int_{0}^{2\pi} d\beta_\nu \int_{C_+} \sin\alpha_\nu \, d\alpha_\nu f_j(\boldsymbol{k_\nu}) g_j(\boldsymbol{k_\nu}) = f_\uparrow^\nu \, g_\uparrow^\nu$$

i.e., the domain of integration is represented by an arrow and the index of the material parameters are indicated by the superscript. In this notation Eqs. (A.6) and (A.7) are written

$$\boldsymbol{E}^{inc}(\boldsymbol{r}) = \boldsymbol{\Phi}_\downarrow^0(\boldsymbol{r}) a_\downarrow^0$$
$$\boldsymbol{E}^{sc}(\boldsymbol{r}) = \boldsymbol{\Phi}_\uparrow^0(\boldsymbol{r}) b_\uparrow^0$$

Within the layer both up and down going waves exist whereas in the lower half-space only down going waves can exist since the half-space is

now assumed to be homogeneous and a radiation condition is assumed at infinity. In the new notation these fields are

$$\begin{aligned}\boldsymbol{E}^1(\boldsymbol{r}) =&\boldsymbol{\Phi}^1_{\downarrow}(\boldsymbol{r})\alpha^1_{\downarrow} + \boldsymbol{\Phi}^1_{\uparrow}(\boldsymbol{r})\beta^1_{\uparrow}\\ \boldsymbol{E}^2(\boldsymbol{r}) =&\boldsymbol{\Phi}^2_{\downarrow}(\boldsymbol{r})\alpha^2_{\downarrow}\end{aligned}$$

Once more the null-field approach provides an algorithm to solve for the unknown fields. In symbolic form the relations can be written as

$$\begin{cases} a^0_{\downarrow} =i(Q^{01}_{\downarrow\downarrow}\alpha^1_{\downarrow} + Q^{01}_{\downarrow\uparrow}\beta^1_{\uparrow})\\ b^0_{\uparrow} = -\, i(Q^{01}_{\uparrow\downarrow}\alpha^1_{\downarrow} + Q^{01}_{\uparrow\uparrow}\beta^1_{\uparrow})\end{cases} \tag{A.8}$$

$$\begin{cases} \alpha^1_{\downarrow} =iQ^{12}_{\downarrow\downarrow}\alpha^2_{\downarrow}\\ \beta^1_{\uparrow} = -\, iQ^{12}_{\uparrow\downarrow}\alpha^2_{\downarrow}\end{cases} \tag{A.9}$$

The Q-functions introduced above are defined as

$$\begin{aligned}Q_{jj'}(\boldsymbol{k}_\nu, \boldsymbol{k}_{\nu+1}) =&2k_\nu \int_{S_\nu} \hat{n}_\nu \cdot \{[\nabla' \times \boldsymbol{\Phi}^\dagger_j(\boldsymbol{k}_\nu;\boldsymbol{r}')] \times \boldsymbol{\Phi}_{j'}(\boldsymbol{k}_{\nu+1};\boldsymbol{r}')\\ &+ C_\nu \boldsymbol{\Phi}^\dagger_j(\boldsymbol{k}_\nu;\boldsymbol{r}') \times [\nabla' \times \boldsymbol{\Phi}_{j'}(\boldsymbol{k}_{\nu+1};\boldsymbol{r}')]\}\, dS'_\nu\,,\ \nu = 0, 1\end{aligned}$$

where $C_\nu = \mu_\nu/\mu_{\nu+1}$. The explicit derivation of equations (A.8) and (A.9) is given in [4]. These equations (A.8) and (A.9) can be solved formally to yield

$$\begin{aligned} b^0_{\uparrow} =&R^T_{\uparrow\downarrow}a^0_{\downarrow}\\ \alpha^1_{\downarrow} =&[1 - R^{11}_{\downarrow\uparrow}R^{11}_{\uparrow\downarrow}]^{-1}T^{10}_{\downarrow\downarrow}a^0_{\downarrow}\\ \beta^1_{\uparrow} =&R^{11}_{\uparrow\downarrow}[1 - R^{11}_{\downarrow\uparrow}R^{11}_{\uparrow\downarrow}]^{-1}T^{10}_{\downarrow\downarrow}a^0_{\downarrow}\\ \alpha^2_{\downarrow} =&T^T_{\downarrow\downarrow}a^0_{\downarrow}\end{aligned} \tag{A.10}$$

where $R^T_{\uparrow\downarrow}$ and $T^T_{\downarrow\downarrow}$ are the total reflection and transmission coefficients of the whole layer and the others are transmission and reflection coefficients of the individual interfaces.

A.3 Complete model

To form the complete model the models in subsections A.1 and A.2 have to be combined. To achieve this the transformations between

the spherical vector waves and the plane vector waves are introduced (cf., e.g., [5])

$$\boldsymbol{\Phi}_j(\boldsymbol{k};\boldsymbol{r}) = \sum_n B^{\dagger}_{nj}(\hat{k})\boldsymbol{v}^i_n(k\boldsymbol{r}) \tag{A.11}$$

$$\boldsymbol{v}^e_n(k\boldsymbol{r}) = 2\sum_j \int_0^{2\pi} d\beta \int_{C_{\pm}} \sin\alpha\, d\alpha B_{nj}(\hat{k})\boldsymbol{\Phi}_j(\boldsymbol{k};\boldsymbol{r})\,,\ z \neq 0 \tag{A.12}$$

The presence of the scatterer in region 2 implies that in addition to down going plane waves up going plane waves have to be introduced, in the region between the scatterer and the plane interface, in order to meet the boundary conditions. Thus Eq. (A.9) now reads

$$\begin{cases} \alpha^1_{\downarrow} = i(Q^{12}_{\downarrow\downarrow}\alpha^2_{\downarrow} + Q^{12}_{\downarrow\uparrow}\beta^2_{\uparrow}) \\ \beta^1_{\uparrow} = -\, i(Q^{12}_{\uparrow\downarrow}\alpha^2_{\downarrow} + Q^{12}_{\uparrow\uparrow}\beta^2_{\uparrow}) \end{cases} \tag{A.13}$$

With the use of the transformations (A.11) and (A.12) the equations (A.2) and (A.3) can be written

$$B^{2\dagger}_{n\downarrow}\alpha^2_{\downarrow} = iQ^e_{nn'}\alpha_{n'} \tag{A.14}$$

$$\beta^2_{\uparrow} = -\,2iB^2_{\uparrow n}Q^i_{nn'}\alpha_{n'} \tag{A.15}$$

If these equations ((A.8), (A.13), (A.14) and (A.15)) are solved formally the fields in the different regions are obtained as

$$\begin{aligned} \boldsymbol{E}_0(\boldsymbol{r}) &= \boldsymbol{E}^{inc}_0(\boldsymbol{r}) + \boldsymbol{E}^{regional}_0(\boldsymbol{r}) + \boldsymbol{E}^{anom}_0(\boldsymbol{r}) \\ &= \boldsymbol{E}^{inc}_0(\boldsymbol{r}) + \boldsymbol{\Phi}^0_{\uparrow}R^T_{\uparrow\downarrow}a^0_{\downarrow} + \boldsymbol{\Phi}^0_{\uparrow}(\boldsymbol{r})T^T_{\uparrow\uparrow}B^2_{\uparrow n}T_{nn'}c_{n'} \end{aligned} \tag{A.16}$$

$$\begin{aligned} \boldsymbol{E}_1(\boldsymbol{r}) &= \boldsymbol{E}^{regional}_1(\boldsymbol{r}) + \boldsymbol{E}^{anom}_1(\boldsymbol{r}) \\ &= \left[\boldsymbol{\Phi}^1_{\uparrow}(\boldsymbol{r})R^{11}_{\uparrow\downarrow} + \boldsymbol{\Phi}^1_{\downarrow}(\boldsymbol{r})\right]\left[1 - R^{11}_{\downarrow\uparrow}R^{11}_{\uparrow\downarrow}\right]^{-1}T^{10}_{\downarrow\downarrow}a^0_{\downarrow} + \\ &\quad + \left[\boldsymbol{\Phi}^1_{\uparrow}(\boldsymbol{r}) + \boldsymbol{\Phi}^1_{\downarrow}(\boldsymbol{r})R^{11}_{\downarrow\uparrow}\right]\left[1 - R^{11}_{\uparrow\downarrow}R^{11}_{\downarrow\uparrow}\right]^{-1}T^{12}_{\uparrow\uparrow}B^2_{\uparrow n}T_{nn'}c_{n'} \end{aligned} \tag{A.17}$$

$$\begin{aligned} \boldsymbol{E}_2(\boldsymbol{r}) &= \boldsymbol{E}^{regional}_2(\boldsymbol{r}) + \boldsymbol{E}^{anom}_2(\boldsymbol{r}) \\ &= \boldsymbol{\Phi}^2_{\downarrow}(\boldsymbol{r})T^T_{\downarrow\downarrow}a^0_{\downarrow} + \left[\frac{1}{2}\boldsymbol{v}^e_n(k_2\boldsymbol{r}) + \boldsymbol{\Phi}^2_{\downarrow}(\boldsymbol{r})R^T_{\downarrow\uparrow}B^2_{\uparrow n}\right]T_{nn'}c_{n'} \end{aligned} \tag{A.18}$$

Here the T matrix is the solution of Eq.(A.5). Furthermore, the amplitude c_n, defined as

$$c_n = 2iQ^e_{nn'}\alpha_{n'}$$

is the solution of

$$c_n + A_{nn'}c_{n'} = d_n$$

$$d_n = 2B^{2\dagger}_{n\downarrow}T^T_{\downarrow\downarrow}a^0_{\downarrow}$$

$$A_{nn'} = -2B^{2\dagger}_{n\downarrow}R^T_{\downarrow\uparrow}B^2_{\uparrow n''}T_{n''n'}$$

References

1. Arfken, G., *Mathematical Methodsfor Physicists,* Academic Press, Inc., Orlando, 3rd ed., 1985.
2. Björkberg, J., and G. Kristensson, "Electromagnetic scattering by a perfectly conducting elliptic disk," *Canadian Journal of Physics,* Vol. 65, No. 7, 723–734, 1987.
3. Dennis, J. E., and R. B. Schnabel, *Numerical Methods for Unconstrained Optimization and Nonlinear Equations,* Prentice-Hall, Inc., Englewood Cliffs, 1983.
4. Karlsson, A., and G. Kristensson, "Electromagnetic scattering from subterranean obstacles in a stratified ground," *Radio Science,* Vol. 18, No. 3, 345–356, 1983.
5. Kristensson, G., "Electromagnetic scattering from buried inhomogeneities– a general three-dimensional formalism," *Journal of Applied Physics,* Vol. 51, No. 7, 3486–3500,1980.
6. Oldenburg, D. W., "Practical strategies for the solution of large-scale electromagnetic inverse problems. *Radio Sci.,* Vol. 29, No. 4, 1081–1099, 1994.
7. Varadan, V. K., and V. V. Varadan, eds., *Acoustic, Electromagnetic, and Elastic Wave Scattering–Focus on the T-Matrix Approach,* Pergamon Press, New York, 1980.
8. Waterman, P. C., "Symmetry, unitarity, and geometry in electromagnetic scattering. *Physical Review D,* Vol. 3, No. 4, 825–839, 1971.